An S-Band Radar Method for Early Detection of Stealth Fighters in Air-to-Air Combat

Ahmet Güngör PAKFILIZ

Dept. of Electrical and Electronics Engineering, University of Turkish Aeronautical Association, Bahçekapı Mahallesi, Okul Sokak, No:11, Türkkuşu Kampüsü, Etimesgut, 06790, Ankara, Turkey

agpakfiliz@thk.edu.tr

Submitted March 22, 2026 / Accepted August 14, 2026 / Online first September 18, 2026

Abstract. *Stealth aircrafts reduce the detection ranges of traditional radar systems primarily by lowering Radar-Cross-Section (RCS) optimized for high-frequency X-band threat radars. To evaluate multi-band detection potential under airframe constraints, this study analyzes the integration of a wing-leading-edge S-band radar array to complement conventional nose-mounted X-band systems. Using link-budget modeling and simulation, detection performance across L-, S-, and X-bands is compared for low-observable target profiles under clear and jamming conditions. The analytical findings indicate that while nose-mounted X-band radars maintain high angular resolution, S- and L-band arrays provide extended burn-through and crossover detection ranges against stealth targets. Specifically, a fixed-aperture S-band wing-mounted configuration offers a balanced trade-off between element density and aperture constraints, providing actionable theoretical insights for future multi-band radar architectures in air-to-air scenarios.*

Keywords

Stealth fighters, air-to-air radar, radar absorbent material, S-band radar

1. Introduction

Stealth technology is designed to minimize the radar, IR, acoustic, and visual signatures of combat aircraft to avoid enemy detection, improve survivability, and enable surprise. Stealth technology has transformed the dynamics of aerial combat and reconnaissance. In response to this technological advancement, military forces worldwide are actively exploring new methods to better detect and counter stealth threats. The most critical and challenging part of stealth is achieving a low radar cross-section (RCS). This is because radars can detect conventional aircraft from several hundred miles away, giving defenders plenty of warning. In comparison, IR, acoustic, and visual sensors typically have much shorter detection ranges [1].

The key technologies for achieving low-RCS fighters span several critical fields. First, it involves developing advanced composite materials and fabrication processes for large load-bearing structures in both aircraft and engines. Second, using advanced radar-absorbing materials (RAMs) and optimizing their application are essential. Third, developing devices and techniques for accurate RCS measurement, along with significantly improved computers and advanced computer-aided design tools, plays a vital role in shaping aircraft structures. Finally, implementing advanced fly-by-wire and computer-controlled electronic flight control systems is required to ensure stability for aerodynamically unstable, low-RCS designs.

The systems identified as potential counter-stealth methods include passive and multi-static radars, low-frequency radars, over-the-horizon radars, and sensitive IR sensor systems [2]. Among the possible options, using low-frequency radars would be an effective solution for fighters' early warning and situational awareness. Unlike traditional nose-mounted radar systems, L- and S-band radars operate at longer wavelengths, which allows them to counter the stealth features of advanced aircraft. In this context, mounting L-band radar systems on fighter aircraft’s wing leading edges has drawn considerable interest and has been implemented on the Su-57. Stealth fighters are designed to dodge shorter radar waves, but longer ones can reveal their location—even if only roughly. While L-band detection may not always guide missiles directly, it helps alert pilots to the presence of a hidden object. By leveraging principles of radar wave propagation and scattering and accounting for RAM's lower efficiency at these frequencies, L-band radar has the potential to provide longer detection ranges and improved situational awareness for identifying low-observable targets, including stealth aircraft.

An essential factor influencing a radar's ability to detect a target is the RCS. The definitions and formulas for RCS show that its value is closely linked to the signal frequency, the object's shape, and the properties of the reflective surface material. The higher a target's RCS, the easier it is for radar to detect it, or in other words, the greater the target's visibility. Stealth aircraft, often called "radar-

DOI: 10.13164/re.2026.0425

invisible," naturally have low radar visibility at certain frequencies. The main reason is that achieving a consistent, low RCS across the entire frequency spectrum for an object, such as an aircraft, is impractical, as RCS varies with frequency [3], [4]. In the absence of RAM usage, the RCS tends to decrease across radar bands from high to low frequencies [5].

RCS primarily depends on frequency. Consequently, it is usually minimized within the radar's operational frequency range that one aims to avoid. Fighter aircraft are essential in air combat. The nose radars carried by these fighter aircraft operate in the X-band, primarily to meet the required detection/tracking precision and resolution, given constraints on size, weight, power, and cooling [6]. Additionally, fire-control radars for ground-based air defense systems operate in the C- and X-bands for similar reasons. Hence, the RCS of a stealth aircraft, designed to evade radar detection, is kept as low as possible in the X-band. In this study, the increase in X-band RCS of a stealth aircraft with optimized RCS is examined as frequency decreases. Subsequently, an S-band radar, designed for integration into the wing section of an F-16 fighter jet, is proposed. The detection range of a stealth fighter aircraft equipped with this radar is investigated, compared with that of L- and X-band radars, and the potential additional advantages and disadvantages are evaluated.

It would be beneficial to incorporate L-band radar on the leading edges of fighter aircraft wings to detect stealth aircraft, in addition to the X-band nose radar. The combined use of X- and L-band radars has been demonstrated with the Byelka radar system on Su-57 fighters [7]. This system includes the nose-mounted N036-1-01 X-band AESA radar with 1522 Tx/Rx modules, two smaller N036B-1-01 X-band AESA radars with 358 Tx/Rx modules on the sides of the forward fuselage, and two N036L-1-01 L-band arrays on the wing's leading-edge extensions. These arrays function as IFF (Identification Friend or Foe) and for detecting stealth aircraft. Computer processing of signals from both radar types enables detection of key targets, such as hostile stealth aircraft.

By comparing traditional nose-mounted radar systems with the proposed method, the research seeks to clarify the strengths and weaknesses of each across different operational scenarios. By filling this critical knowledge gap, the study aims to offer valuable insights to military planners, radar engineers, and defense policymakers navigating the complexities of modern air combat.

The introduction of stealth aircraft has transformed traditional aerial warfare, requiring a shift in detection and tracking methods. Conventional radar systems, designed to detect high-RCS targets, face significant challenges in detecting stealth aircraft that employ advanced materials and aerodynamic designs to reduce their radar signatures. Thus, there is an urgent need to explore new radar technologies to degrade the stealth capabilities of these hard-to-find enemies.

S- and L-band radars are compelling options due to their distinctive operational characteristics. They operate at longer wavelengths than the more common X-band or Ku-band radars used on nose-mounted systems, resulting in improved penetration through adverse weather and dense foliage. It is also better at detecting stealth targets with lower RCS [4]. Furthermore, the extended range of S- and L-band radar enables more comprehensive coverage and the identification of targets at greater distances, enhancing situational awareness and providing more time for assessment and response.

Recent advances in counter-stealth research increasingly emphasize multi-spectrum integration, intelligent detection networks, and adaptive electromagnetic surface engineering to overcome low-observable defenses. Early intelligent radar detection frameworks have demonstrated the utility of networked architectures for optimizing target visibility in complex operational environments [8]. Furthermore, modern stealth platforms use adaptive multispectral metamaterials and neural network-driven designs to dynamically manipulate target signatures across multiple frequency bands [9]. To counter these evolving threats, recent radar detection architectures—including reconfigurable intelligent surface (RIS)-assisted systems—have been proposed to improve detection performance for low-RCS targets [10]. Building on these multi-frequency and adaptive paradigms, there is an urgent need for airborne platform-integrated solutions that explicitly leverage physical aperture limitations and cross-band RCS signatures.

Overall, S- and L-band radars show strong potential to improve fighter aircraft capabilities in aerial surveillance, interception, and air dominance. Open-source reports indicate that the Su-57 uses the same antenna arrays for the IFF system and L-band early detection of stealth aircraft; however, a full operational performance report on the L-band radar has not yet been released. Additionally, no dedicated S-band airborne radar specifically designed to counter stealth aircraft has been documented in the literature.

This study proposes an S-band radar design, in addition to the conventional X-band nose radar, to detect stealth aircraft before engagement. Unlike standard multi-band radar approaches in the literature—which typically deploy separate sensors simultaneously for data fusion or target classification without structural optimization—the proposed concept introduces a targeted physical and parametric countermeasure. The framework’s novelty lies in deliberately exploiting the Mie scattering transition region exhibited by modern low-observable platforms, specifically in the 3 GHz spectrum [11].

While conventional X-band designs suffer from heavy reliance on radar-absorbent materials and the specular deflection of stealth geometries, the proposed configuration captures the resonance-driven radar cross-section (RCS) anomalies of the target. By structurally balancing the array geometry (a 20-element S-band array versus a 12-

element L-band baseline), the layout is shown to circumvent the severe frequency-squared path loss inherent to higher bands. Consequently, the proposed architecture retains 93% of the maximum detection range of a lower-frequency surveillance radar while providing the superior angular resolution and Doppler characteristics necessary for early-stage tracking, effectively bridging the operational gap between tactical fire control and wide-area surveillance.

L- and S-band radar systems do not dynamically adjust their physical array apertures to exploit the structural resonance of stealth targets. Their performance in detecting stealth aircraft within formations is systematically evaluated, addressing several key research questions: (*i*) how the RCS of a stealth fighter varies as frequency shifts from the X to the S and L bands; (*ii*) the relative detection ranges of L- and S-band radars compared with nose-mounted radar systems against stealth aircraft across various operational environments; and (*iii*) the extent to which factors such as atmospheric conditions and target features influence the effectiveness of L- and S-band radar systems in detecting stealth aircraft.

By exploring these questions, this research contributes to the ongoing discussion on enhancing airborne surveillance and reconnaissance amid the growing development of stealth technology. Its findings are expected to inform future advancements in radar systems, tactical operations, and defense strategies, helping military forces adapt more effectively to evolving threats and sustain air superiority in challenging environments.

The core methodology and analytical validation developed in this work align directly with current research in advanced radar engineering. To explicitly highlight the novelty of this study relative to the state-of-the-art (SOTA), the main contributions are summarized as follows:

- ***Unified Cross-Band Link Budget Framework (Benchmarked against Single-Band SOTA):*** Unlike conventional radar link budget formulations that assume a single frequency or use simplified target RCS models, this work establishes a high-fidelity, parametric cross-band framework. This model rigorously incorporates frequency-dependent path-loss penalties and non-ideal atmospheric degradation, enabling a direct, realistic comparison of X-, S-, and L-band capabilities for low-observable targets.
- ***Full-Wave Electromagnetic Validation of Compact Apertures (beyond Idealized Array Assumptions):*** While existing airborne counter-stealth literature predominantly relies on isotropic or idealized antenna assumptions, this work presents a full-wave electromagnetic simulation of a realistic 20-element S-band patch microstrip array. It confirms that a 3 GHz carrier can achieve weapon-quality tracking precision while fully respecting tight airborne platform footprint constraints.
- ***Conservative Counter-Stealth EW Assessment under Realistic Threats:*** Unlike standard Electronic Counter-Countermeasure (ECCM) evaluations that assume generic target RCS profiles, the proposed architecture's performance bounds are rigorously evaluated against low-observable targets under active electronic countermeasures, demonstrating superior signal-to-jamming (S/J) resilience even with conservative threat parameters.

The paper is organized as follows: Section 2 outlines the theoretical foundations of RCS for a stealth fighter and RAM. Section 3 describes the location of the L-band radar antenna. Section 4 discusses the L-band radar design for the proposed method. Section 5 presents a simulation study comparing range-detection analyses for X-, S-, and L-band radars. The paper concludes with a summary in Sec. 6.

2. Theoretical Foundations

2.1 RCS of a Fifth-Generation Stealth Fighter

The advances in computer technology during the 1970s enabled successful computer simulations, thereby proving the concept of a stealth fighter aircraft. These studies led to the development of the F-117A, B-2, and B-1B, often regarded as the three emblematic stealth aircraft of the late '80s [12]. Recognizing the capabilities of stealth technology, the pioneer stealth aircraft, primarily the F-117, inspired the development of fifth-generation fighters. These stealth fighters, categorized by role and RCS-reduction features, can be outlined across several modern platforms.

To assess the proposed S-band detection architecture against typical low-observable (LO) threats, we selected three operational fifth-generation fighters as benchmark target platforms: the F-35, Su-57, and J-20. While open-source RCS data for these advanced platforms is limited, existing operational evaluations provide insights into their unique design philosophies and LO characteristics [13], [14].

The F-35 is considered a standard Western stealth platform, featuring extensive RCS reduction capabilities [14]. In contrast, the Russian Su-57 emphasizes a balance between aerodynamic agility and front-hemisphere RCS reduction, with an estimated average RCS ranging from 0.1 to 1 m², as noted in patent RU2502643 C2 [15]. Including both the Su-57 and J-20 alongside the F-35 allows for a thorough multi-spectral RCS baseline across the L-, S-, and X-bands for our simulation framework.

During the F-35 fighter jet's design phase, its RCS is meticulously optimized. This phase involves comprehensive computer simulations that balance aerodynamic efficiency with stealth considerations in the aircraft's exterior design. Every surface is carefully shaped to minimize RCS while meeting aerodynamic demands. Features such as flattened surfaces and sharp edges are used to reduce radar wave scattering and reflection [16]. In areas where aerodynamic performance is more important than RCS reduction,

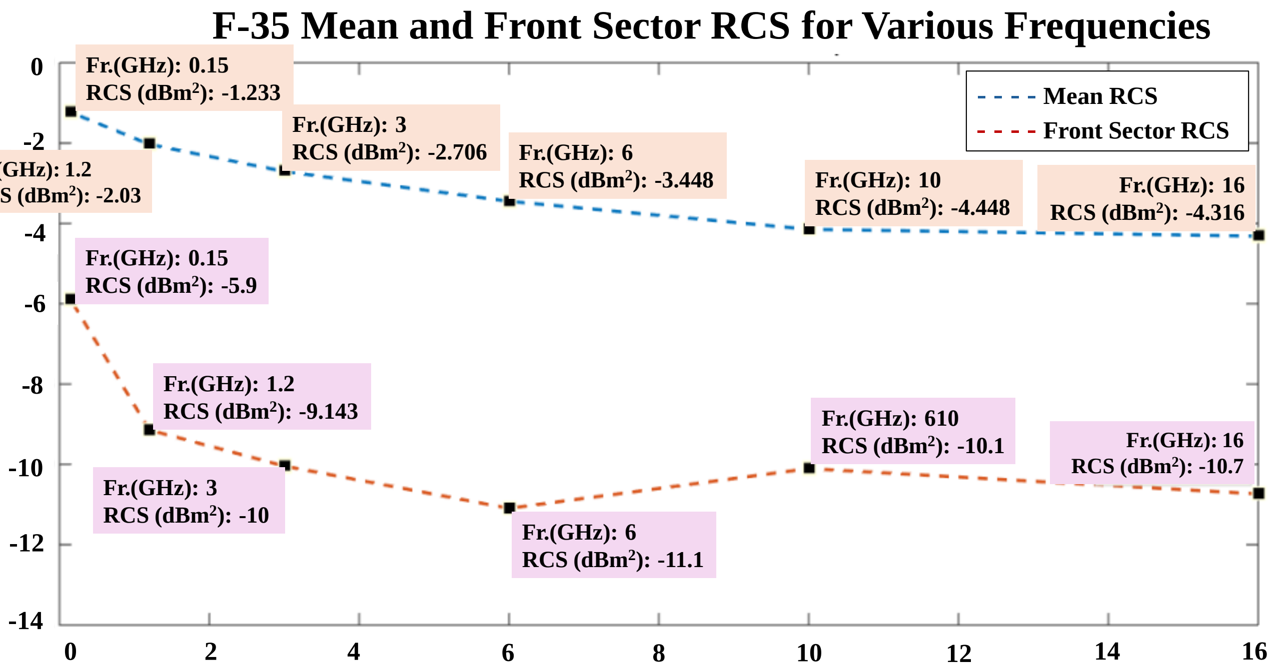

Fig. 1. Sample F-35 mean and front-sector RCS at various frequencies.

radar-absorbing materials are used. The entire exterior of the aircraft is also coated with radar-absorbing paint to enhance its stealth capabilities.

Calculating the aircraft's RCS is challenging due to the lack of a physical aircraft model, the difficulty of obtaining material information even when a model exists, and the high computational and memory demands of full-wave or asymptotic solvers. Figure 1 shows the RCS analysis of the F-35 [17]. In the RCS analysis study, the aircraft's 3D model was created using advanced 3D modeling software. During development, data were collected from open-source photos and videos; comparison data were used to estimate actual dimensions; official statements, promotional brochures detailing wingspan and size, expert opinions, and comparisons with similar aircraft were also used.

The F-35 model developed in this study was processed using the POFACETS algorithm and subjected to multiple simulations. Notably, the simulation model did not include RAM coating. The simulations were performed over an azimuth range of −30° to 30° around the aircraft's nose and an elevation range of −15° to 15°. The azimuth resolution was set to 1° and the elevation resolution to 5° within the VHF-Ku band.

The analysis includes both the frontal-sector RCS and the mean RCS. For target detection, evaluating the frontal-sector RCS, which corresponds to the monostatic scanning radar's aspect, yields more accurate results than the average RCS.

In this context, the frontal-sector RCS without RAM material is −10.1 dBm^2, and it is stated that with the material, this value would decrease to −20 dBm^2. However, the material properties are not discussed in this study; therefore, the material used in later chapters is used to determine the frontal-sector RCS. The simulation results are shown in Tab. 1.

Freq (GHz)	Front Sector RCS (dBm^2)	Mean RCS (dBm^2)
1.2	−9.143	−2.031
3	−10.04	−2.706
6	−11.09	−3.448
10	−10.1	−4.147
16	−10.73	−4.316

Tab. 1. Geometry-based RCS analysis results of F-35.

2.2 Radar Absorber Materials in Fighters

RAM and Radar-Absorber Paints (RAP) are applied to combat aircraft surfaces to suppress specular radar reflections by converting incident RF energy into heat [5]. These materials—ranging from tuned-frequency absorbers to surface-wave absorbers—are engineered primarily to optimize absorption within the conventional nose-radar operational frequency band (8–12 GHz) [18], [19].

However, a critical performance limitation of standard RAM configurations is their narrow frequency response. As shown in Figs. 2–4 and Tab. 2, the reflectivity curves of representative materials (MR11-0010-00, MR31-0003-00, and MF-500) demonstrate that high absorption efficiency (up to −27 dB) is achieved in the X-band, whereas performance degrades noticeably at lower frequencies, such as the L- and S-bands [20]. This frequency-dependent attenuation gap provides the physical rationale for evaluating lower-frequency radar detection capabilities.

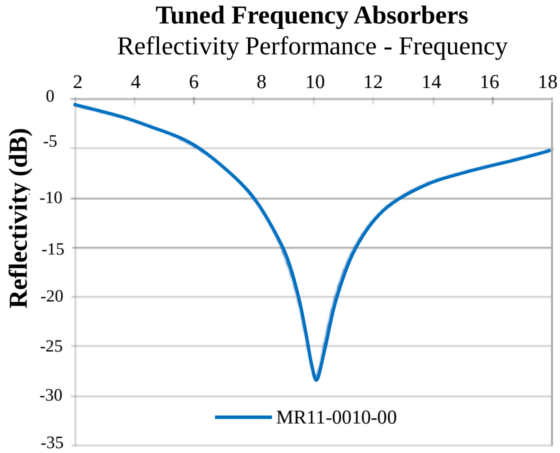

Fig. 2. MR11-0010-00 reflectivity performance.

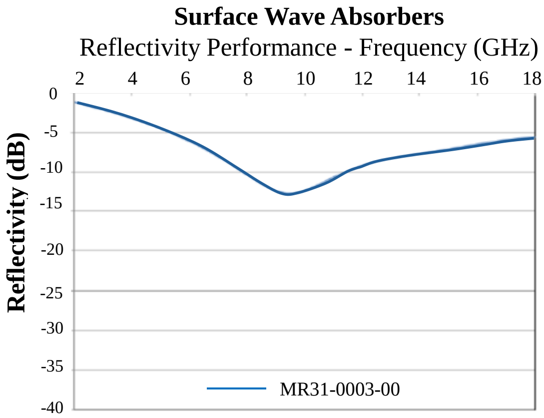

Fig. 3. MR31-0003-00 reflectivity performance.

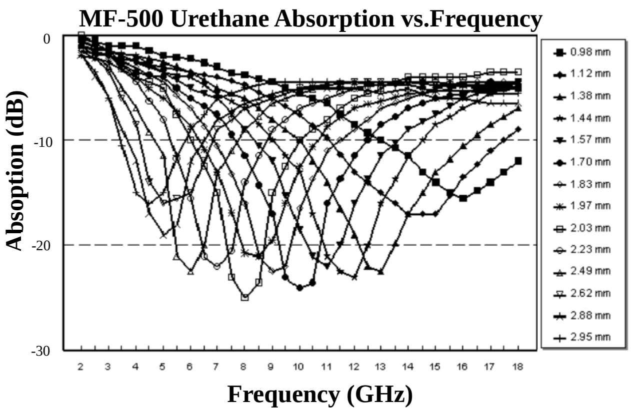

Fig. 4. MF-500 absorption performance up to frequency.

Frequency (GHz)	Material Type		
	MR11-0010-00 Reflectivity (dB)	**MR31-0001-00 Reflectivity (dB)**	**MF-500 (thickness: 1.97 mm) Reflectivity (dB)**
1.2	−1	−1	−2
3	−2	−2	−3
10	−27	−13	−15

Tab. 2. Reflective performances of the materials according to frequency.

2.3 The Effect of the Materials on the RCS

The estimated RCS of the F-35 in Fig. 1 is based solely on its geometry. However, because the aircraft is coated with RAM materials, these coatings will influence its RCS. The final RCS estimate incorporates the materials listed in Tab. 2. To determine an $\bar{\sigma}_{@1.2\text{ GHz}}$ overall average, the absorption properties of these materials have been averaged. At 1.2 GHz and 3 GHz, the combined average RCS reduction performance of the three materials is as follows:

$$\begin{aligned}\bar{\sigma}_{@1.2\text{ GHz}} &= \frac{10^{-0.2}+10^{-0.1}+10^{-0.1}}{3} = 0.74 \rightarrow -1.3\text{ dB},\\ \bar{\sigma}_{@3\text{ GHz}} &= \frac{10^{-0.3}+10^{-0.2}+10^{-0.2}}{3} = 0.58 \rightarrow -2.3\text{ dB}.\end{aligned} \tag{1}$$

On the other hand, at 10 GHz, the combined average performance of the three materials is given by (2):

$$\bar{\sigma}_{@10\text{ GHz}} = \frac{10^{-1.4}+10^{-2.7}+10^{-1.3}}{3} = 0.03 \rightarrow (-15\text{ dB}). \tag{2}$$

By adding the average improvement in RAM material to the average frontal RCS values listed in Tab. 1, the total RCS of the F-35 is obtained, as shown in Tab. 3. This table details the frontal-sector RCS values at 1.2, 3, and 10 GHz. The wide frequency range leads to a significant difference in target detection distances between L- and X-band radars, with a disparity of 15.816 dB in RCS. Conversely, the RCS difference between S-band and X-band is 14.147 dB.

The RCS values of the Su-57 and J-20 fighters can be approximated relative to the F-35's RCS at the same frequencies. These relative ratios are approximated from open sources and reports. In this context, the assumptions for the front sectors are presented in Tab. 4 [21], [22].

3. The Radar's Antenna Location

This study selects the F-16 Fighting Falcon as the attack aircraft model. The analysis focuses on mounting the

Frequency (GHz)	Front Sector RCS (dBm^2)	Mean RCS (dBm^2)
1.2	−10.443	−3.331
3	−12.34	−5
10	−25.1	−19.147

Tab. 3. F-35 RCS with material.

Frequency Band	Su-57 RCS/F-35 RCS		J-20 RCS/F-35 RCS	
	Ratio	**dB**	**Ratio**	**dB**
L-band	1.85	2.67	1.2	0.8
S-band	4	6	1.8	2.55
X-band	11.34	10.54	3.1	4.93

Tab. 4. Su-57 and J-20 RCS ratio relative to F-35 RCS.

L-band radar antenna on the F-16. Initially, using open-source information, an estimated X-band radar detection range is determined based on the existing antenna. The importance of the X-band radar is recognized because the L-band radar will support the X-band fire control radar system. Subsequently, an appropriate location for the L-band radar antenna is identified, taking into account the F-16's structure and dimensions.

3.1 The X-Band Radar

Radar detection range is a critical parameter for fighter aircraft and is therefore highly classified. Because the diameter of the radar antenna is also important for indirect detection range estimation, exact dimensions are often not disclosed. However, open sources report that the diameter of the AN/APG-83 nose radar used in F-16 Block 70 versions is approximately 60-70 cm. This data is usually inferred from publicly available photos and videos. Range estimates for the AN/APG-83 from open sources are typically presented within the context of such studies.

The AN/APG-83 nose radar is expected to provide a detection range of 47 NM (87 km) for a target with a 1 m² RCS [23]. Therefore, detection ranges for an F-16 equipped with the AN/APG-83 nose radar for various RCS targets can be estimated using the high-PRF (pulse repetition frequency) radar equation in (3) [24]:

$$R_{\text{max}} = \left[\frac{P_{\text{Tx}}\ d_{\text{t}}\ G^2\ c^2\ \sigma\ T_{\text{i}}}{(4\pi)^3\ f^2 k\ T_0\ F\ \text{SNR}\ L} \right]^{\frac{1}{4}} \tag{3}$$

where R_{max} is the maximum detection range in km, P_{Tx} is the transmitter (Tx) power in watts, d_{t} is the transmit duty factor, G is the monostatic radar antenna gain (unitless), c is the speed of light (3×10^8 m/s), f is the operating frequency in Hz, σ is the target RCS, and T_{i} is the radar integration time (or time-on-target), which is the reciprocal of the Rx bandwidth ($1/B$). The denominator also includes Rx sensitivity, which comprises the noise floor (kT_0B), noise figure (F), and signal-to-noise ratio (SNR).

3.2 The L-Band Radars

Fighters can operate at both very low and very high altitudes. For example, an F-16's service ceiling can range from 50 meters at low level to 50,000 ft. However, sustained flights at these extremes can strain aircraft materials due to environmental conditions and degrade engine performance because of limited oxygen. Therefore, fighters usually engage at altitudes between 20,000 and 35,000 ft during combat. Because the likelihood of air-to-air engagement drops at very high and very low altitudes, lateral resolution is more important than vertical resolution in aircraft design. As a result, an L-band radar intended for installation should have a horizontal antenna array rather than a vertical one.

The optimal placement for this radar is on the wing leading edges, providing frontal visibility and supporting horizontal installation. To determine an appropriate antenna size for this region, the F-16 aircraft's dimensions were first examined, with particular focus on the leading-edge length. Figure 5 shows the dimensions of the F-16 aircraft [25].

The length of the wing's leading edge was calculated from the leading-edge angle in the image and the specified wingspan. Figure 6 presents the wing's leading-edge angle and the wing dimensions.

In Fig. 6, the length of the leading edge (L) is calculated using the Pythagorean theorem to be 4.02 m, as follows:

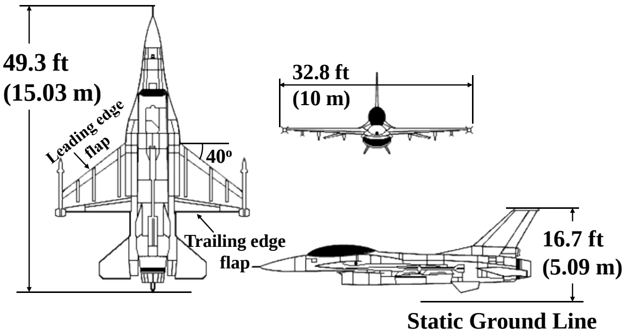

Fig. 5. Dimensions of F-16 Fighter Falcon.

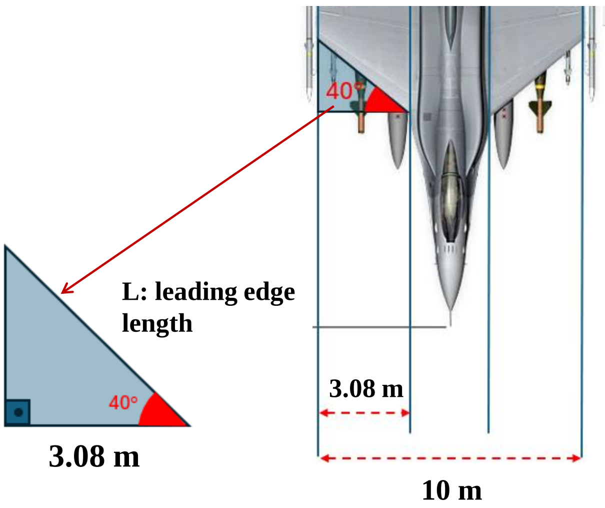

Fig. 6. Dimensions of the wing's leading-edge.

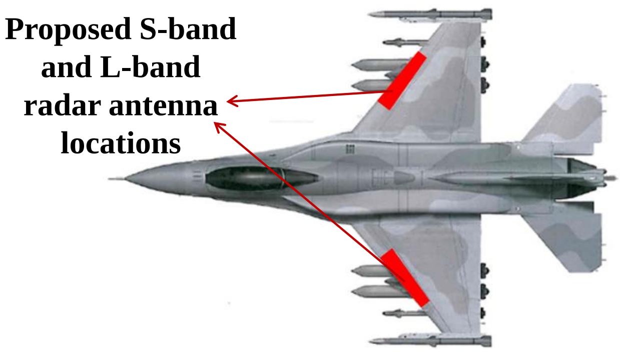

Fig. 7. The proposed S- and L- band antenna locations.

$$L = \frac{3.08\ \text{m}}{\cos\left(40^{\circ}\right)} = 4.02\ \text{m}. \quad (4)$$

Based on these calculations, the proposed installation sites for the aircraft's S- and L-band radars are deemed suitable for placement along the wing's leading edge. Figure 7 illustrates the conceptual placement options.

4. Proposed S-band and Conceptual L-Band Radar Design

This section describes the design process for the proposed L-band radar. It assesses the detection-range performance of the X-band radar currently used by F-16 fighters, using publicly available range data. The L-band radar is a system envisioned in this study, and its range estimates are based on the design and selection of its subcomponents during development.

4.1 The X-Band Radar Detection Range

In the previous section, the detection range of an F-16 Block 70 fighter jet for a target with an RCS of 1 m² was provided. However, since this study focuses on an F-35 fighter as the target, the radar detection range is calculated using the radar range equation (3). Because the only parameters that change in the radar range equation for these two targets are their RCS values, it suffices to calculate using the RCS ratios.

The F-35's RCS is first converted to a linear scale. The impact of this ratio on the detection range is then calculated using the fourth root of the RCS ratio. Applying this formula, the detection range is 28.794 km. Based on these calculations, the F-16 Viper fighter can detect targets at the following ranges with a 90% probability of detection (P_D), given the specified RCS values. Table 5 presents a comparison of the results.

4.2 The L- and S-Band Radar Analysis

This study examines the L-band and S-band radar mounted on the leading edge of the F-16 fighter aircraft's wing. A single-element linear array antenna is chosen for the wing leading edge due to thickness limitations. The antenna, with a length *d* designed for the specific area, will have a particular power-aperture product (PAP). A radar system with a higher PAP will be more effective at detecting stealth fighters compared to the nose radar. The PAP depends on gain and power, as shown in the following formula:

$$\text{PAP} \propto \frac{P_{\text{Tx}} G^2}{F}. \quad (5)$$

Research on suitable power amplifiers for L- and S-band applications has been conducted, in which P_{Tx} denotes the output power, *G* denotes the monostatic radar antenna gain, and *F* denotes the noise figure [24].

	Reference Target	F-35
RCS (m^2)	1	0.012
Range (km)	87	28.794

Tab. 5. AN/APG-83 detection range for different RCS values.

4.2.1 L-Band and S-Band RF Power Amplifiers

This section reviews various L- and S-band power amplifiers (PAs) available on the market, designed specifically for L- and S-band radar systems. The objective is to assess and compare these amplifiers to identify the best fit for seamless integration into the system. It highlights key technical specifications and strategic considerations for choosing the right amplifier, supporting the development of airborne radar technology.

When choosing a power amplifier for military use, it is important to consider key factors that ensure top performance and reliability in tough environments. These include robustness, efficiency, dependability, and compatibility with existing systems. Durability guarantees the amplifier can endure harsh conditions, such as extreme temperatures, vibrations, and shocks common in military operations. Efficiency is vital for reducing power consumption and extending battery life, allowing for longer field deployments.

Reliability guarantees consistent performance over time, reducing the risk of downtime or malfunctions during critical missions. Compatibility with existing systems allows smooth integration and interoperability with other military equipment. By carefully evaluating RF PAs against these criteria, military users can choose the most suitable option for their operational needs. For L-band, MACOM's CGHV14800 is a good PA operating within the 1.2–1.4 GHz frequency range. It is a gallium nitride (GaN) high-electron-mobility transistor (HEMT) designed for high efficiency, high gain, and wide bandwidth, making it ideal for power amplification.

Conversely, RFHIC's RRP27311K0-22 is an appropriate choice for S-Band radar. It is a GaN HEMT amplifier with high efficiency and power, operating between 2.7 GHz

	Type of the RF PA	
Parameters	**CGHV14800**	**RRP27311K0-22**
Frequency (GHz)	1.2	2.7
Gain (dB)	15.5	22 (Typical)
Output Power (W)	1000	1000 (Typical)
Frequency (GHz)	1.4	3.1
Gain (dB)	15.1	22 (Typical)
Output Power (W)	910	1000 (Typical)

Tab. 6. RF power amplifiers specification summary.

and 3.1 GHz. As noted in its datasheet, this amplifier can be used in radar systems [26], [27]. The datasheet specifications are summarized in Tab. 6.

4.2.2 Antenna Design for the L- and S-Band Radars

The antenna, designed to be mounted on the leading edge of the F-16 wing, will be a single-row, electronically scanned linear antenna that delivers azimuthal resolution. Phased-array linear antennas are essential in radar systems, especially in L-band applications where flexible beam steering and high resolution are vital. This section discusses the design and analysis of these antennas, focusing on key parameters and their respective formulas.

Phased-array linear antennas are essential components of radar systems, especially for L-band applications where flexible beam steering and high-resolution capabilities are crucial. This approach can also be applied to S-band applications, which are not yet widely used. This section covers the design and analysis of these antennas, focusing on key parameters and their related formulas.

The main factors influencing a radar's Figure of Merit (FoM) are output power and antenna gain. Both are directly related to the linear array length, denoted by *d*. As the antenna length increases, the antenna gain and output power also increase, depending on the number of elements [28].

In phased-array antennas, element spacing and scan angles are constrained to prevent grating lobes. These antennas, which use phase shifters to control multiple elements and enable electronic scanning in various directions, produce unintended sidelobes called grating lobes that appear in directions other than the main beam. The grating lobes of electronically scanned phased-array antennas depend on the wavelength and the range of scanning angles. They result from the spacing between elements or from the number of antenna elements [29], [30].

To prevent or minimize grating lobes, careful design of the antenna array layout is crucial. The key restriction that blocks unwanted signals that could impair performance depends on the element spacing. This spacing should be at least $\lambda/2$. For a frequency of 1.2 GHz, the maximum element spacing to avoid grating lobes is 0.125 meters, and spacings are chosen accordingly. At 3 GHz, the maximum is 0.05 meters. The second restriction involves steering the main beam. The formula below, with d denoting the spacing and θ the scan angle, shows how to avoid grating lobes [31]:

$$d_{\max} < \frac{\lambda}{1+\left|\cos\left(\theta_{\max}\right)\right|}. \tag{6}$$

This rule implicitly sets the maximum number of antenna elements in the array. To prevent grating lobes up to 40 degrees, the spacing between antenna elements must be less than 0.1416 meters at 1.2 GHz. The calculation shows that the chosen spacing of 0.125 m satisfies this requirement. Additionally, the 3 GHz design requires a maximum spacing of 0.057 m; the selected 0.05 m spacing is therefore appropriate. The number of antenna elements and power amplifiers determines the array's total output power. The pattern multiplication theorem describes the far-zone field pattern of an antenna array. It states that the propagation pattern of N identical antennas, one with a pattern of $F_e(\theta)$, is obtained by multiplying it by $F_a(\theta)$, the pattern of the array when all elements are replaced with isotropic antennas. The theorem is outlined as follows.

$$F\left(\theta\right) = F_e\left(\theta\right) \times F_a\left(\theta\right). \tag{7}$$

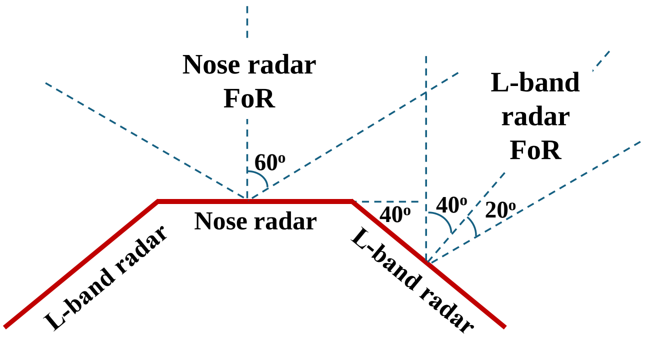

Fig. 8. FoRs demonstration of nose and L-band radar.

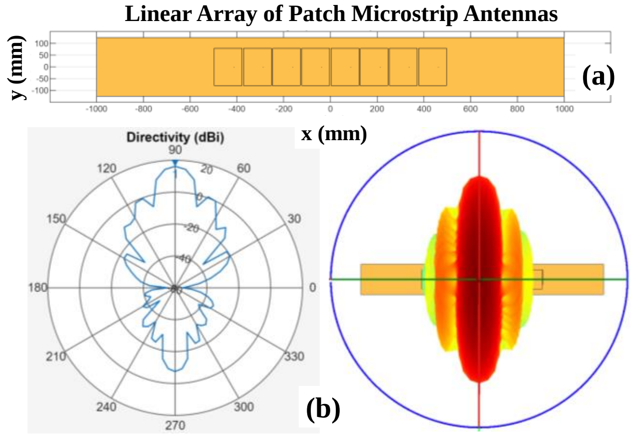

Fig. 9. (a) Physical demonstration of the L-band array with 8 elements, and (b) its 2-d and 3-d directivity pattern in the plane normal to the array.

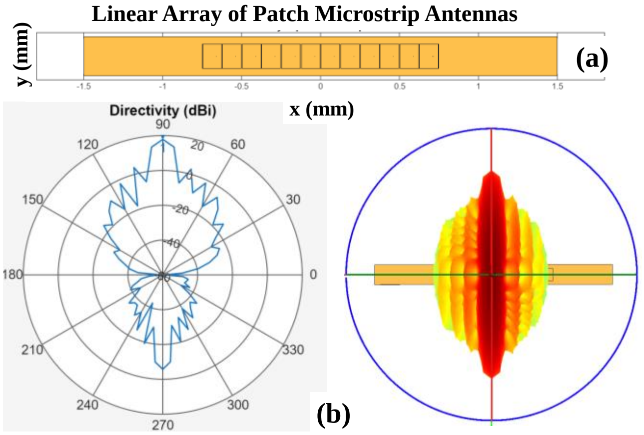

Fig. 10. (a) Physical demonstration of the L-band array with 12 elements, and (b) its 2-d and 3-d directivity pattern in the plane normal to the array.

For the array antenna design, the requirements include high gain without grating lobes and a proper fit to the wings' leading edges. To achieve this, a linear array of patch microstrip antennas has been chosen. As a minimum, an eight-element antenna array is selected for both L- and S-band radar configurations. MATLAB's Array Designer was used. Figure 9 shows the physical shape and dimensions of the 8-element L-band (1.2 GHz) antenna array, along with the directivity pattern in the plane perpendicular to the array. The L-band 8-element patch microstrip array, spaced 0.125 m apart, exhibits a peak directivity of 16.2 dBi. The antenna elements are approximately 1 m long, and the substrate is about 2 m long. Considering the appropriate mounting dimensions on the wings (4.02 m), another configuration uses 12 elements to increase the antenna gain and output power.

The 12-element patch microstrip array, with elements spaced 0.125 m apart, shows a peak directivity of 17.83 dBi. The antenna elements are roughly 1.5 m long, and the substrate is about 3 m long. For the S-band (3 GHz) design, the minimum number of antenna elements is set to 8, similar to the L-band design.

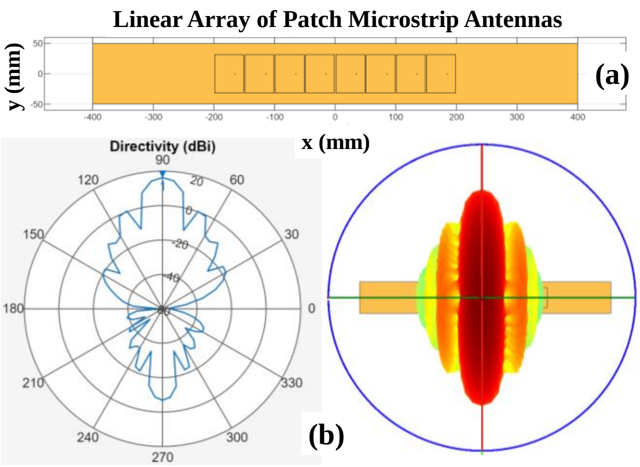

Fig. 11. (a) Physical demonstration of the S-band array with 8 elements, and (b) its 2-d and 3-d directivity pattern in the plane normal to the array.

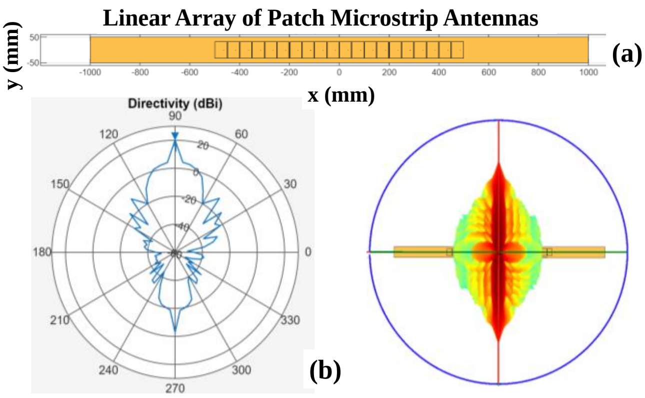

Fig. 12. (a) Physical demonstration of the S-band array with 20 elements, and (b) its 2-d and 3-d directivity pattern in the plane normal to the array.

Figure 11 displays the physical shape and dimensions of the 8-element S-band antenna array, along with the directivity pattern in the plane perpendicular to the array. The S-band 8-element patch microstrip array, spaced 0.05 m apart, has a peak directivity of 16.3 dBi. The antenna elements are roughly 0.4 m long, and the substrate is about 0.8 m long. This fits the appropriate mounting dimensions on the wings (4.02 m).

Another configuration utilizes 20 elements to enhance antenna gain and output power. Figure 12 displays the physical shape and dimensions of the 20-element S-band (3 GHz) antenna array, along with the directivity pattern in the plane normal to the array.

The 20-element S-band patch microstrip array, with elements spaced 0.05 m apart, achieves a peak directivity of 20.1 dBi. The antenna elements are roughly 1 m long, and the substrate is about 2 m long. The relationship between directivity and antenna gain is defined as:

$$G = e_0 \times D \tag{8}$$

where $e_0 = e_{cd} \times e_r$, G represents the realized gain (or simply the antenna gain), and D is the directivity. Additionally, e_0 is the total efficiency, which includes the antenna radiation efficiency, e_{cd}, and the reflection efficiency, e_r. In this study, the overall efficiency is assumed to be 80%, which realistically accounts for dielectric and conductor losses in practical microstrip layouts.

4.2.3 Comparative Analysis with Established Radar Mosaics

To rigorously validate the performance of the proposed S-band radar configuration, a quantitative comparative analysis is conducted against two established, industry-standard baseline radar designs operating in adjacent frequency bands: a long-range L-band surveillance radar and a fire-control X-band radar. All systems are evaluated under an identical operational scenario featuring an incoming low-observable (stealth) target with a nominal RCS of $\sigma = 0.01\ \mathrm{m}^2$ (or −20 dBm²) moving through a standard atmospheric environment with rain attenuation (R = 5mm/h).

As dictated by the R_{max} equation (3), the maximum detection range is governed by the intricate interplay between the square of the operational frequency (f^2) in the denominator and the frequency-dependent target RCS (sigma) in the numerator. When transitioning from the proposed S-band (3 GHz) to the X-band (10 GHz), the system incurs a severe 10.45 dB penalty due to the f^2 factor (in the denominator) alone. Concurrently, as shown in Tab. 7, the front-sector average RCS of the F-35 target decreases by 12.76 dB (from −12.34 dBm² to −25.1 dBm²). This cumulative degradation in the link budget significantly limits the X-band R_{max} for early-stage stealth detection.

Based on the summary in Tab. 7, the proposed S-band framework effectively bridges the operational gap between L- and X-band systems for low-observable platforms.

Parameter	L-Band Baseline (12-element array)	Proposed S-Band (20-element array)	X-band Baseline
Operating frequency (f)	1.2 GHz	3 GHz	10 GHz
Target RCS (σ) [F-35]	–10.443 dBm^2	–12.34 dBm^2	–25.1 dBm^2
Target RCS (σ) [Su-57]	–7.773 dBm^2	–6.34 dBm^2	–14.68 dBm^2
Target RCS (σ) [J-20]	–9.643 dBm^2	–9.79 dBm^2	–21.12 dBm^2
Required Threshold SNR	14 dB	14 dB	14 dB
Freq. Penalty (f^2)	1.44 × 10^{18}	9 × 10^{18}	100 × 10^{18}
Atmospheric & Rain Attenuation (L_a)	Negligible	Very low	Severe / High vulnerable
Relative Detection Range	1.0 × (Baseline)	0.93 ×	0.37 ×

Tab. 7. Cross-band link budget and validation matrix.

On the other end of the spectrum, while the L-band minimizes the f^2 penalty, it requires a prohibitively large physical antenna aperture (A_e) to maintain a narrow beamwidth, making it unsuitable for versatile tactical deployments. Therefore, the proposed 3 GHz framework exploits a physical 'sweet spot' where the target's stealth geometry exhibits transitional scattering anomalies (yielding significantly higher RCS values than at X-band) while avoiding the operational footprint of lower-frequency surveillance radars.

5. Simulation Study

This section assesses the performance of preliminary designs for the L- and S-band radar systems through a simulation study. The simulation aims to determine the detection range between the attacker (an F-16) and stealth targets such as the F-35, Su-57, and J-20. Although in an air-to-air engagement, the predator might become prey, roles are not interchangeable in this study. Both non-jamming and jamming conditions are examined.

Since the exact operational specifications of the Su-57's N036L-1-01 L-band radar are classified, the simulated L-band system in this study serves as a theoretically bounded representative model. The parameters are modeled using established radar-equation constraints, subject to airborne volume and power limitations. To ensure the validity of the comparison, a sensitivity analysis was conducted by varying the radar parameters, confirming that the over- or underestimation of the exact platform metrics does not alter the fundamental conclusions of the comparative analysis.

The study evaluates antenna arrays with 8 and 12 elements for L-band and with 8 and 20 elements for S-band radars. The 8-element array is identified as the minimum requirement, while other configurations depend on the wing's allowable dimensions. Additionally, weather conditions are considered, with separate assessments for clear weather and varying rainfall scenarios.

To ensure reproducibility and technical benchmarking of the results presented, all electromagnetic, radar cross-section (RCS), and signal processing simulations were run on a high-performance computing workstation. The hardware (HW) architecture consists of an Intel(R) Core i7-7700 processor (3.60 GHz clock speed, equipped with 8 logical processors via Hyper-Threading technology), 32 GB of RAM, and dedicated HW acceleration. On the software side, high-fidelity electromagnetic modeling and physical layout configurations were performed using the MATLAB Antenna Array Designer tool (Version R2025a), while complex radar range equations, signal processing algorithms, and multi-band comparative predictive analytics were developed and executed in MATLAB (Version R2025a).

5.1 Performance Comparison for Non-Jamming, Non-Precipitation Conditions

For comparison, Equation (3) is rearranged to clarify the relationship between SNR and range (R) as follow:

$$\mathrm{SNR} = \frac{P_{\mathrm{Tx}}\ d_{\mathrm{t}}\ G^2\ c^2\ \sigma\ T_{\mathrm{i}}}{(4\pi)^3 R^4 f^2\ k\ T_0\ B\ F\ L\ L_{\mathrm{a}}}. \tag{9}$$

To evaluate and compare the detection performance of different radar regimes against low-RCS targets, three

Parameter (Symbol)	L-Band Radar	S-Band Radar	X-band Radar
Operating Frequency (f)	1.2 GHz	3 GHz	10 GHz
Peak Tx Power (P_{Tx})	8 kW (8-el.) 12 kW (12-el.)	8 kW (8-el.) 20 kW (12-el.)	10 kW
Duty Factor (d_t)	0.2	0.2	0.2
Radar Rx BW (B)	5 MHz	5 MHz	5 MHz
Antenna Directivity (D)	16.2 dBi (8-el.) 17.83 dBi (12-el.)	16.3 dBi (8-el.) 20.1 dBi (20-el.)	25 dBi
Antenna Total Efficiency (e_0)	0.8	0.8	0.8
Total Radar Losses (L)	4 dB	4 dB	4 dB
Radar Integration Time (T_i)	8 ms	8 ms	8 ms
Temperature (T)	330 K	330 K	330 K
Noise Figure (F)	3 dB	3 dB	3 dB
Atmospheric Loss (L_a)	0.0001 dB/km (no precip.)	0.002 dB/km (no precip.)	0.008 dB/km (no precip.)

Tab. 8. Technical specifications of the radar systems.

Frequency (GHz)	F-35 (dBm^2)	Su-57 (dBm^2)	J-20 (dBm^2)
1.2	−10.443	−7.773	−9.643
3	−12.34	−6.34	−9.79
10	−25.1	−14.68	−21.12

Tab. 9. Front sector average RCS values of the target fighters.

distinct radar systems operating in the L-, S-, and X-bands were modeled. The comprehensive technical specifications, including peak transmit power configurations for varied element arrays, antenna directivities, receiver bandwidths, and environmental loss parameters for each radar band, are detailed in Tab. 8.

Based on Tab. 3 and 4, the front-sector RCS values for the target fighters are defined and presented in Tab. 9. These values are used in the simulations.

The performance comparison is conducted under no-rain atmospheric attenuation conditions, with a focus on boresight antenna gain. For this purpose, the atmospheric-loss assumptions described above are used, and trials are conducted between the existing X-band nose radar and the L-band and S-band 8-element antenna-array radar proposals. The detection SNR is calculated using the Albersheim equation [32]. Thus, the probability of detection (P_D) is set to 94%, the probability of false alarm (P_{FA}) to 10^{-7}, and the SNR to 14 dB. The SNR-versus-detection-range plots for the F-35s are shown in Fig. 13.

As shown in Fig. 13, using an 8-element antenna array expands the detection range for the F-35 fighter by 8.62 km for the L-band radar and 2.04 km for the S-band radar. The simulations were conducted separately for each target fighter.

The results of these simulations are shown in Tab. 10. In the 8-element antenna array trials, the L-band radar outperforms the others. However, this isn't ideal, as not all of the antenna array's capacity is used, especially for the S-band radar. In the second comparison study, the S-band radar has 20 elements, while the L-band radar has 12. This

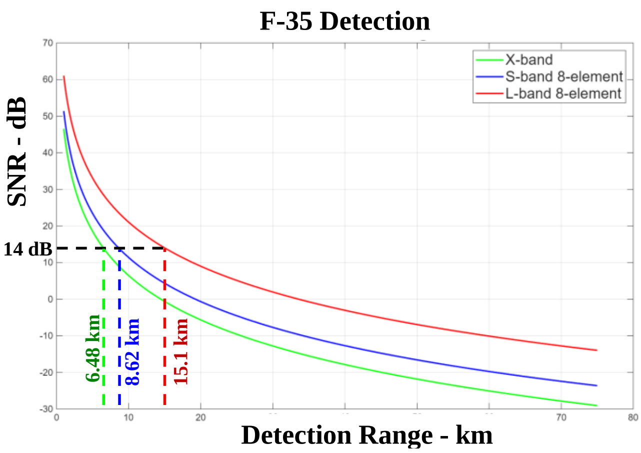

Fig. 13. SNR versus detection range curves for the F-35 by X-, S-, and L-band radars.

Target Fighter	X-Band Radar Detection Range (km)	S-Band Radar Detection Range (km)	L-Band Radar Detection Range (km)
F-35	6.48	8.62	15.1
Su-57	17.5	11.81	12.18
J-20	8.2	10	15.7

Tab. 10. X-band, S-band, and L-band radar detection ranges for 8-element antenna arrays.

difference results from variations in the dimensions and spacing of the antenna elements, which depend on frequency.

The SNR-versus-detection-range plots for the Su-57 fighter are shown in Fig. 14. As shown, using a 12-element antenna array for the L-band radar and a 20-element array for the S-band radar converges the detection ranges of the two radars. The detection ranges of the L- and S-band radars nearly fully overlap, and both extend detection by about 6 km beyond the X-band radar, enhancing detection for the Su-57 fighter.

The simulations for this condition were conducted separately for each target fighter. The results of these simulations are shown in Tab. 11.

Table 11 shows that the improvement in detection range at high power and high antenna gain is impressive, as expected. In the S-band, more antenna elements can be packed into a smaller volume than in the L-band, as shown in Tab. 11. Using S-band radar separates IFF from the early stealth-detection radar. This adds HW to the system; however, the volume would be similar to that in the L-band case.

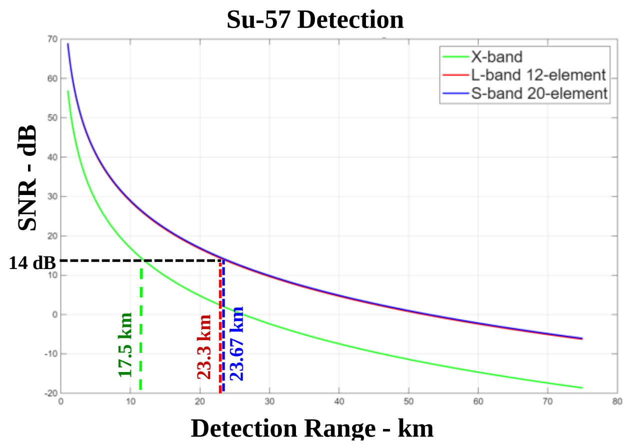

Fig. 14. SNR versus detection range curves for the Su-57 by X-, S-, and L-band radars.

Target Fighter	X-Band Radar Detection Range (km)	S-Band Radar (20-element array) Detection Range (km)	L-Band Radar (12-element array) Detection Range (km)
F-35	6.48	16.8	20
Su-57	17.5	23.67	23.3
J-20	8.2	19.6	20.92

Tab. 11. X-band, S-band, and L-band radar detection ranges.

Additionally, the need for time-sharing disappears, allowing continuous, uninterrupted operation. The detection range increase for the F-35 fighter is 13.52 km from L-band to X-band and 10.32 km from S-band to X-band. The detection range improvements for the J-20 are 11.5 km for S-band and 12.82 km for L-band.

5.2 Performance Comparison under Rain

Different frequency bands exhibit varying attenuation behavior due to rain. Therefore, it is useful to analyze how X-, S-, and L-band radars perform under different rain conditions. This section explores the impact of rain on radar performance, using the attenuation curves shown in Fig. 15 [33].

Based on the graphs shown in Fig. 15, Table 12 is prepared. It displays rain attenuation as a function of frequency, derived from measurements in the L-, S-, and X-bands. Trials for various rain-load effects are conducted solely on the F-35 fighter. Figure 16 displays the SNR versus detection range for the extreme case of a rain rate of 16 mm/hr.

In this scenario, detection ranges are 6.1 km for the X-band radar, 8.5 km for the S-band 8-element array radar, and 15 km for the L-band 8-element array radar.

Table 13 shows the detection ranges of the X-band, S-band 8-element array, and L-band 8-element array radars against an F-35 under different rain conditions. The detection range of the L-band radar is more prominent than in open-air conditions.

As shown in Tab. 13, the variations across all rain loads are very minor at the L- and S-bands; the variation at

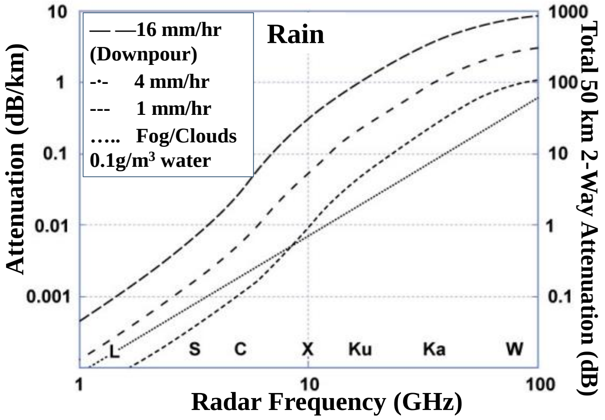

Fig. 15. Attenuation caused by different precipitation rates with respect to the frequency elements.

Radar Operating Frequency (GHz)	Rain rate, mm/hour		
	16	4	1
1.2	0.001	0.0005	0.0002
3	0.008	0.004	0.0007
10	0.15	0.018	0.01

Tab. 12. Rain attenuation rates.

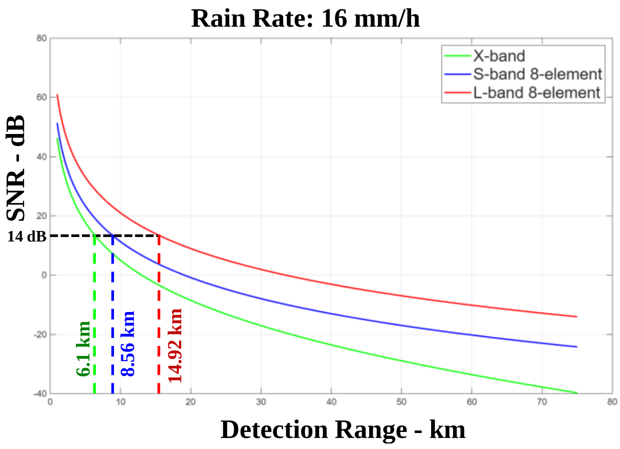

Fig. 16. SNR versus detection range curves for X-band, S-band, and L-band 8-element array radars for F-35 and a rain rate of 16 mm/hr.

Rain Rate (mm/hr)	X-Band Radar Detection Range (km)	S-Band Radar (8-element array) Detection Range (km)	L-Band Radar (8-element array) Detection Range (km)
1	6.47	8.6	15
4	6.4	8.58	14.94
16	6.1	8.56	14.92

Tab. 13. X-band, S-band, and L-band radar detection ranges for F-35 under different rain loads.

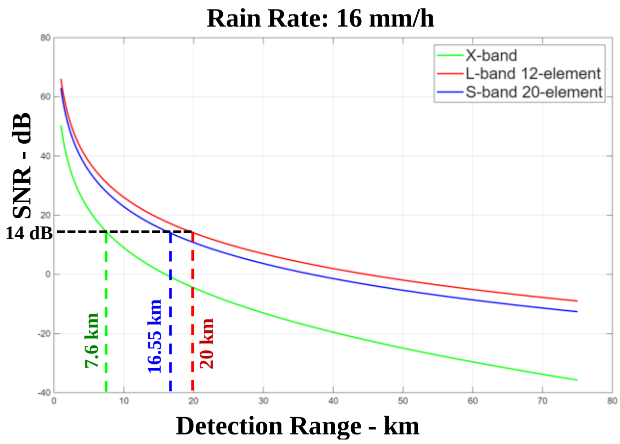

Fig. 17. SNR versus detection range curves for X-band, S-band 20-element array, and L-band 12-element array radars for J-20 and a rain rate of 16 mm/hr.

Rain Rate (mm/hr)	X-Band Radar Detection Range (km)	S-Band Radar (20-element array) Detection Range (km)	L-Band Radar (12-element array) Detection Range (km)
1	8.12	19.51	20.91
4	8.1	19.44	20.9
16	7.6	19.37	20.8

Tab. 14. X-band, S-band, and L-band radar detection ranges for J-20 under different rain loads.

the X-band radar is relatively higher compared to the others. In the 8-element array case, the power and antenna gains are inadequate.

For the L-band 12-element array and S-band 20-element array radar conditions, the detection ranges for the J-20 fighter are shown in Fig. 17. Once again, the figure highlights the most effective scenario: rain rate of 16 mm/hr. As shown in Fig. 17, Table 14 displays the detection ranges of the X-band, S-band 20-element array, and L-band 12-element array radars against a J-20 aircraft under various rain loads. At a 16 mm/hr rain rate, the L-band radar's detection range increases by 12.4 km, and the S-band radar's by 8.95 km, relative to the X-band radar's detection range.

As shown in Tab. 14, across all rain loads, the variations are very slight at the L- and S-bands; the variation at the X-band radar is relatively high compared to the others. In the 20-element array case, S-band radar detection performance improves and approaches that of the L-band radar.

5.3 Performance Comparison under Jamming

To complete the overall performance analysis, it would be helpful to include jammer signals. For this purpose, the analysis focuses on the stealth fighters' self-protection systems operating in repeater-noise jamming mode [34]. Deceptive jamming is outside the scope of this study. Additionally, another assumption underlies the jamming analysis. Conventional SPJ systems are highly efficient and power-optimized for higher-frequency threats, such as those in the 6-20 GHz range. They show a severe drop in jamming efficiency against lower-frequency targets. However, this property of current SPJ systems is ignored in the analysis. Although SPJ usage against the L and S bands is not prevalent, it will be required in the future to protect stealth aircraft. In the jammer analysis, performance is assessed using the signal-to-jamming ratio (S/J), as shown in the following equation [24]:

$$\frac{S}{J} = \frac{P_{Tx}\ d_t\ G\ \sigma\ B_J L_J}{P_J\ G_J \left(4\pi\right) R^2 L_R}. \tag{10}$$

The purpose of the equation is to establish a relationship between the S/J ratio and range (R). The radar and RCS values are consistent with those used in previous simulation studies for the L- and S-band wing radars and the X-band nose radar. The jammer-related components of (10) can be defined as:

Jammer power in (P_J): 100 W

Jammer antenna gain (G_J): 3.16 (ratio) or 5 dB

Jammer losses (L_J): 2.512 ratio or 4 dB

Jammer operating bandwidth (B_J): 50 MHz

The jamming performance comparison is conducted without accounting for atmospheric attenuation and focuses on the boresight antenna gain. As with previous tests, the trials involve the existing X-band nose radar, the L-band 8-element and 12-element antenna-array radars, and the S-band 8-element and 20-element antenna-array radar proposal. The purpose of earlier trials was to determine the detectable SNR range. This time, however, the comparison of radar performance depends on the burn-through range and crossover range. The burn-through range is the distance from the radar to the target at which the target's return signal becomes detectable despite jamming. It is usually just beyond the crossover range, where J equals S [24].

The initial evaluation used an 8-element array spanning the L- and S-bands to assess F-35, Su-57, and J-20 target platforms under repeater-noise self-protection jamming (SPJ). Figure 18 shows the resulting S/J trajectory versus range for the jammed F-35 platform. Because calculated burn-through ranges remained below 1.5 km—rendering detection impractical for operational air-to-air engagements—the analysis focuses strictly on crossover ranges, summarized in Tab. 15. Under heavy jamming, where frequency-dependent stealth advantages diminish, detection performance is governed primarily by radar transmit power, target RCS, antenna gains, and the receiver-to-jammer bandwidth ratio. Consequently, targets with lower X-band RCS (F-35 and J-20) yield reduced crossover ranges, whereas the Su-57's higher frontal RCS corresponds to the maximum crossover extent across the evaluated bands.

When the L-band radar uses a 12-element antenna and the S-band radar uses a 20-element antenna, their power and antenna gain increase. These improvements are expected to enhance the SPJ system's ability to detect stealth fighters. The results for each fighter are shown in Fig. 19.

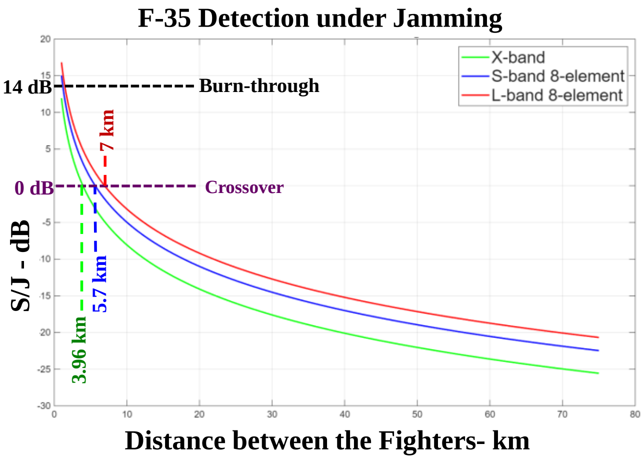

Fig. 18. S/J versus detection range curves for X-band, S-band, and L-band 8-element array radars for F-35.

Fighter	X-Band Radar Crossover Range (km)	S-Band Radar (8-element array) Crossover Range (km)	L-Band Radar (8-element array) Crossover Range (km)
F-35	3.96	5.7	7
Su-57	13.2	11.4	9.5
J-20	6.2	7.8	7.7

Tab. 15. X-band, S-band, and L-band crossover ranges.

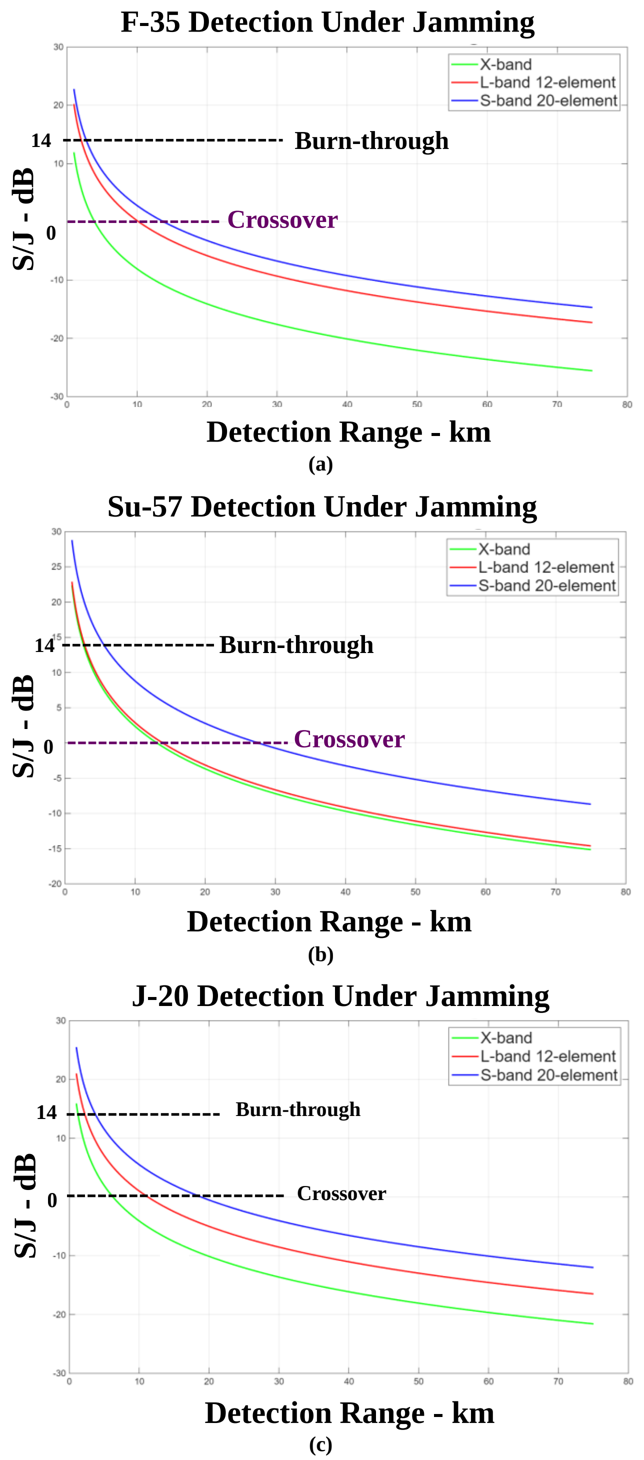

Fig. 19. S/J versus detection range curves of X-band, S-band 20-element, and L-band 8-element array radars for (a) F-35, (b) Su-57, and (c) J-20.

Fighter	X-Band Radar Crossover Range (km)	S-Band Radar (20-element array) Crossover Range (km)	L-Band Radar (12-element array) Crossover Range (km)
F-35	4	14	10.2
Su-57	13.2	27.7	14.1
J-20	6.2	19.3	11.4

Tab. 16. X-band, S-band, and L-band crossover ranges.

Target Fighter	X-Band Radar Detection Range (km)		S-Band Radar (20-element array) Detection Range (km)		L-Band Radar (12-element array) Detection Range (km)	
	w/o-J	w-J	w/o-J	w-J	w/o-J	w-J
F-35	6.48	0.85	16.8	2.8	20	2.1
Su-57	17.5	2.75	23.67	5.5	23.3	2.77
J-20	8.2	1.25	19.6	3.74	20.92	2.25

Tab. 17. X-band, S-band, and L-band radar detection range comparison with and without jamming.

This time, the maximum burn-through ranges are approximately 2.7 km for the F-35, 5.5 km for the Su-57, and 3.7 km for the J-20, all measured using an S-band radar. Table 15 summarizes the results for the crossover ranges.

Table 16 demonstrates that the S-band radar system's advantage for stealth aircraft is clear. Reaching these crossover ranges with X-band radar requires boosting power, which can be very difficult due to propagation losses. Meanwhile, L-band radar can reach these levels by using more antenna elements, but this is not practical given the wing dimensions.

To evaluate performance under jamming (w-J), the burn-through range (S/J = 14 dB) is compared with the no-jamming baseline (w/o-J) in Tab. 10.

Table 17 confirms that jamming significantly reduces detection ranges, and S-band radar maintains the highest relative performance.

5.4 Discussion on Link Budget and Aperture Trade-offs

To examine the size-versus-range trade-off, a link budget analysis is used. The maximum detection range R_{max} is proportional to the radar aperture, as given by (3). For a phased array antenna with a fixed physical aperture area A, the maximum gain G is directly related to the effective area by $G = 4\pi A/\lambda^2$. When comparing L-band and S-band radar systems within the same spatial volume, the S-band's shorter wavelength ($\lambda_S < \lambda_L$) enables a significantly higher density of antenna elements spaced at $\lambda/2$ intervals.

Consequently, although an individual S-band element is physically smaller, populating the fixed aperture with more elements ($N_S > N_L$) yields a sharp increase in total coherent array gain ($G_{total} \propto N$). This integration scales the overall power-gain product ($P^t \cdot G^2 \cdot \lambda^2$), effectively resolving the aperture-to-wavelength trade-off. When combined with the facts that stealth aircraft exhibit significantly larger non-optimized RCS (σ) in the S-band than in the X-band and that S-band suffers negligible atmospheric attenuation relative to X-band under adverse weather, the comprehensive link budget mathematically supports a longer operational detection range against low-observable targets.

The mathematical correlation behind the sharp increase in the range observed between Tab. 10 and Tab. 11

lies in the spatial element integration capability governed by (3) and the following equation:

$$N \propto \frac{4A}{\lambda^2} \,. \tag{11}$$

In a configuration where the number of elements is artificially held constant ($N = 8$ in Tab. 10), the L-band radar naturally outperforms the S-band due to its lower free-space path loss (FSPL $\propto 1/\lambda^2$). However, this baseline comparison does not reflect practical airborne design constraints, where physical volume or aperture area (A) is the hard limit.

Under a fixed-aperture constraint (Tab. 11), the S-band's shorter operating wavelength ($\lambda_S \approx 10$ cm) allows the array to scale to 20 elements, whereas the L-band's larger footprint ($\lambda_L \approx 25$ cm) limits the grid to 12 elements within the same cross-section. Because the total coherent array gain scales quadratically ($G_{Tx} G_{Rx} \propto N^2$) in the radar link budget, this higher integration density directly offsets the S-band's higher path loss, yielding a 95% range extension for the F-35 target (from 8.62 km to 16.8 km). This analysis fully resolves the trade-off raised during the review process: although a smaller S-band element has lower standalone gain, a fixed-aperture S-band array delivers significantly higher total coherent gain and a superior power-aperture product than an L-band array occupying the same physical space.

5.5 Analytical Discussion and Physical Validation

Due to military classification and the limited availability of 5th-gen stealth aircraft for open-air RCS testing, simulated performance profiles were validated against established theoretical frameworks. The resulting detection ranges across the L-, S-, and X-bands align with fundamental radar-scattering theories. Although modern stealth relies on shaping and RAMs to suppress specular reflections at the high-frequency X-band (where the wavelength is much smaller than aircraft components), their effectiveness naturally degrades at the lower-frequency L-band. In the L-band, the operational wavelength approaches the physical dimensions of key aircraft structures (such as wing edges or control surfaces), shifting the scattering mechanism from the optical to the resonance (Mie) region. Consequently, the comprehensive data below underscore that while nose-mounted X-band radars suffer severe range reduction against low-RCS targets, the integrated use of S-band and L-band radar systems provides a robust, physically validated counter-stealth detection capability across diverse operational and atmospheric environments.

To contextualize this work's contributions within the current state of the art, the main outputs and methodological benchmarks of the proposed multi-band radar framework are systematically compared with recent prominent studies in the literature, as detailed in Tab. 18.

Analysis of the existing literature shows that stealth target detection approaches generally focus either on modeling transient peaks from operational single-band radars during dynamic maneuvers [35] or on highly theoretical quantum radar frameworks [36] that have not yet reached field-deployable TRL levels. By contrast, countermeasure technologies such as multi-band selectively absorbing photonic crystals [37] significantly degrade the steady-state detection probability (P_D) of such single-frequency systems. The proposed S-band-centered multi-band fusion architecture specifically targets resonant vulnerabilities in the damping characteristics of modern threats across multiple bands, effectively leveraging wavelength-to-target-dimension interactions rather than relying solely on transient maneuvering peaks. The computational complexity of the proposed method's multi-band data fusion layers is explicitly documented in Tab. 18; however, simulation results confirm that this overhead remains strictly within real-time operational limits when executed on modern embedded FPGA/GPU HW.

Study	Technology / Perspective	Resistance to Multi-Band RAM	Applicability / TRL Level	Trade-off / Limitations
Lu et al. [35]	Traditional Single-Frequency Radar (Dynamic RCS Peak/Anomaly Analysis)	**Weak:** Although focusing on transient RCS peaks during dynamic maneuvers, it remains insufficient to decipher advanced RAM coatings optimized for single frequencies.	**High TRL:** Based on mathematical modeling of currently operational radar infrastructure and of signal-processing algorithms.	Heavily dependent on transient peaks at specific maneuver angles, it fails to provide a stable, continuous P_D.
Lu et al. [36]	Next-Generation Quantum Radar (Photon Entanglement / Quantum RCS)	**Theoretically High:** Aims to bypass classical electromagnetic absorption and damping limits via quantum states.	**Low TRL:** Confined to laboratory environments due to atmospheric decoherence and thermal noise.	Suffers from severe range limitations in open-air propagation, instability, and very high HW complexity.
Zhang et al. [37]	Multispectral Compatible Metamaterial (Advanced Threat Material Perspective)	**Threat Baseline:** Provides integrated, multispectral camouflage and damping across radar, laser, and infrared bands.	**Medium/High TRL:** Represents newly developed, advanced multispectral stealth metasurfaces currently under development.	Exhibits high manufacturing complexity, and its damping performance is strictly dependent on specific radar aspect angles.
Proposed Method	**Multi-Band RF Signal Fusion** and **Intelligent Detection**	**Strong:** Exploits specific resonance gaps in the S-band backbone to decode the signature of multi-band-absorbing RAM coatings.	**Medium/High TRL:** Deployable in the field through intelligent signal-processing layers integrated into existing active RF HW.	Introduces extra data-fusion layers and a higher computational load than traditional single-band methods.

Tab. 18. Comparison of the proposed work with recent state-of-the-art radar and RCS detection studies.

5.6 Data and Model Availability Statement

The complete mathematical framework and executable MATLAB code files (Fig13.m through Fig19.m) used to generate the detection curves and performance benchmarks in this work are publicly available in the following repository:
https://github.com/ahmetgun1970/S_Band_Stealth_Radar_Simulation

6. Conclusion

The study analyzes the simulation and evaluation of an S- and L-band air radar system mounted on a fighter aircraft's wing, designed to detect stealth aircraft at extended ranges without relying on X-band nose radars. It proposes mounting an S-band radar on fighters to detect stealth aircraft. To this end, the study develops an S-band radar system. Because the specific operational details of the Su-57's N036L-1-01 L-band radar are classified, the study's simulated L-band system serves as a theoretical approximation, as discussed in Sec. 5.

Results indicate that S-band radars perform comparably to L-band radars in both clear weather and rain, while significantly outperforming traditional X-band nose radars against low-observable targets. Specifically, link-budget analyses show that the proposed 20-element S-band array, operating with a simulated peak directivity of 20.1 dBi and a strict 80% radiation-efficiency constraint, retains 93% of the maximum detection range (R_{max}) of a much larger 12-element L-band surveillance array.

Under adverse environmental conditions, the S-band architecture demonstrates strong resilience to atmospheric and rain attenuation (L_a), in sharp contrast to the severe propagation losses suffered by the X-band framework. Furthermore, under identical operational thresholds (SNR = 14 dB), the S-band radar exploits the transitional Mie scattering resonance anomalies of modern stealth airframes, bypassing the steep 12.76 dB drop in target RCS observed when moving from 3 GHz down to 10 GHz on platforms like the F-35.

The quantitative robustness of this approach is further validated under electronic countermeasures. As summarized in Tab. 15 and 16, the S-band framework yields superior crossover ranges compared to X-band and L-band variations in the presence of jamming. These mathematical and electromagnetic parameterizations confirm that increasing the radar's antenna size and element density yields a significantly higher S/J ratio than legacy configurations, confirming that the proposed system meets size, weight, and power (SWaP) requirements while offering a highly feasible, conformal deployment model for fighter wings.

Consequently, the observed operational superiority of the S-band architecture does not stem from a single variable; rather, it arises from a synergistic combination of structural antenna characteristics—where a higher element density directly amplifies the coherent array gain—and electromagnetic resilience, which exploits the lower efficiency and power-splitting constraints of tactical airborne jammers typically optimized for higher-frequency regimes.

Further research in two areas could improve the benefits of the S-band radar system. First, SPJ systems on fighter aircraft typically operate in the 6-20 GHz range. Although radar warning receiver (RWR) systems, which typically operate in the 2-20 GHz band, would detect RF signals from an S-band radar, they would not be jammed. To enable jamming, the mission data files would need to be updated to extend jamming capability up to 2 GHz. This would force the jammer to use its limited power at low frequencies, leaving the fighter vulnerable to C-, X-, and Ku-band threats. Developing more capable SPJ systems for power management should be an important area for further work.

The second benefit of using S-band radar concerns SWaP. Because the L-band radar and IFF interrogator systems operate in the same frequency band and share an antenna, this configuration is beneficial for SWaP. However, radar and IFF cannot operate simultaneously. Implementing an S-band radar system would reduce both antenna size and associated HW. Therefore, S-band radar can meet the same SWaP requirements as L-band radar. Additionally, separate IFF and radar systems would enable simultaneous operation. Further SWaP analysis and practical studies on mounting options for fighter wings are needed to support the deployment of S-band radar.

References

[1] LORELL, M. A., LEVAUX, H. P. The 1970s to the 1990s: The stealth revolution. In *The Cutting Edge: A Half Century of U.S. Fighter Aircraft R&D*. 1st ed. RAND Corporation. 1998. ISBN: 0-8330-2607-0

[2] ZIKIDIS, K., SKONDRAS, A., TOKAS, C. Low observable principles, stealth aircraft and anti-stealth technologies. *Journal of Computations & Modelling*, 2014, vol. 4, no. 1, p. 129–165. ISSN: 1792-7625 (print), 1792-8850 (online)

[3] LYNCH, D. *Introduction to RF Stealth.* Raleigh (NC): Scitech Publishing Inc., 2004. DOI: 10.1049/SBRA120E

[4] ZOHURI, B. *Radar Energy Warfare and the Challenges of Stealth Technology*. Berlin: Springer, 2020. DOI: 10.1007/978-3-030-40619-6

[5] KNOTT, E. F., SCHAEFFER, J. F., TULLEY, M. T. *Radar Cross-Section*. 2nd ed. SciTech Publishing, 2004. ISBN-10: 1891121251

[6] STIMSON, G. W. *Introduction to Airborne Radar*. 2nd ed. SciTech Publishing, 1998. ISBN-10: 1891121014

[7] XU, P., WANG Y., XU X., et al. Structural-electromagnetic-thermal coupling technology for active phased array antenna. *International Journal of Antennas and Propagation*, 2023, no. 1, p. 1–36. DOI: 10.1155/2023/2843443

[8] ZHANG, J. A novel intelligent radar detection network. *Journal of Physics: Conference Series*. IOP Publishing, 2022, p. 1–5. DOI: 10.1088/1742-6596/2181/1/012056

[9] CHEN, W., DUAN, Y., MA, D., et al. Neural network–enabled accelerated discovery of multifunctional metamaterials for adaptive multispectral stealth applications. *Materials Today Physics*, 2025, 52, p. 1–11. DOI: 10.1016/j.mtphys.2025.101696

[10] YAN, L., GAO, Y., COLONE, F., et al. RIS-aided radar detection architectures with application to low-RCS targets. *arXiv preprint arXiv:2601.10846*, 2026, p. 1–17. DOI: 10.48550/arXiv.2601.10846

[11] BOHREN, C. F., HUFFMAN, D. R. *Absorption and Scattering of Light by Small Particles*. John Wiley & Sons, 2008. ISBN: 9783527618163

[12] RICHARDSON, D. *Stealth Warplanes*. Zenith Imprint, 2001. ISBN-10: 0760310513

[13] PELOSI, M. J., KOPP, C. A. Preliminary assessment of specular radar cross section performance in the Sukhoi T-50 prototype. *Air Power Australia Analyses*, 2012. [Online] Cited 2026-03-22. Available at: https://www.ausairpower.net/APA-2012-03.html

[14] BOLKCOM, C. *F-35 Lightning II Joint Strike Fighter (JSF) Program: Background, status, and issues*. 2009. [Online] Cited 2026-03-22. Available at: https://apps.dtic.mil/sti/tr/pdf/ADA494859.pdf

[15] DAVIDENKO, A. N., STRELEC, M. J., GAVRIKOV, A. J., et al. Multifunctional aircraft of decreased radar signature (in Russian). Russia patent RU2502643C2. 2013-12-27. [Online] Cited 2026-03-22. Available at: https://patents.google.com/patent/RU2502643C2/en

[16] PAKFILIZ, A. G. Increasing self-protection jammer efficiency using radar cross section adaptation. *Computers & Electrical Engineering*, 2022, vol. 98, p. 1–19. DOI: 10.1016/j.compeleceng.2021.107635

[17] ZIKIDIS, K. C. Early warning against stealth aircraft, missiles and unmanned aerial vehicles. In Karampelas, P., Bourlai, T. (eds.). *Surveillance in Action: Technologies for Civilian, Military and Cyber Surveillance*. Cham: Springer International Publishing, 2017, p. 195–216. DOI: 10.1007/978-3-319-68533-5_10

[18] MAST TECHNOLOGIES, San Diego, California. *MR11-0010-00 Tuned Frequency Absorber, Silicone.* Datasheet. 2018. [Online] Cited 2026-03-22. Available at: https://www.masttechnologies.com/wp-content/uploads/2016/04/MR11-0010-00-Tech-Data-Sheet.pdf

[19] MAST TECHNOLOGIES, San Diego, California. *MR31-0013-00 Surface Wave Absorber, Silicone*. Datasheet. 2018. [Online] Cited 2026-03-22. Available at: https://www.masttechnologies.com/wp-content/uploads/2016/04/MR31-0003-00-Tech-Data-Sheet.pdf

[20] MWT MATERIALS, Inc., New Jersey. *MF-500-Urethane.* Datasheet. 2020. [Online] Cited 2026-03-22. Available at: https://www.mwtmaterials.com/wp-content/uploads/2020/04/MWT-TD-MF-500-Urethane-Ver-4.2.pdf

[21] ABRAMS, A. *J-20 Mighty Dragon: Asia's First Stealth Fighter in the Era of China's Military Rise*. Helion and Company, 2024. ISBN-10: 1804515604

[22] VUVUZELA. F-35 vs J-20 vs Su-57 RCS. *Aircraft 101*, Jan. 20, 2020. [Online] Cited 2026-03-22. Available at: basicsaboutaerodynamicsandavionics.wordpress.com.

[23] GAITANAKIS, G. K., LIMNAIOS, G., ZIKIDIS, K. C. On the use of AESA (active electronically scanned array) radar and IRST (infrared search & track) system to detect and track low observable threats. In *MATEC Web of Conferences*, 2019, vol. 304, p. 1–8. DOI: 10.1051/matecconf/201930404001

[24] MAHAFZA, B. R. *Radar Signal Analysis and Processing using MATLAB.* Chapman and Hall/CRC, 2016. ISBN: 9780429149337

[25] LOCKHEED MARTIN CORPORATION. *T.O. GR1F-16CJ-1. Flight Manual HAF Series Aircraft F-16C/D.* 2002 [Online] Cited 2026-03-22. Available at: https://info.publicintelligence.net/HAF-F16.pdf

[26] MACOM. *CGHV14800; 800W; 960-1400 MHz GaN HEMT for L-Band Radar Systems*. Datasheet, 2022. [Online] Cited 2026-03-22. Available at: https://cdn.macom.com/datasheets/CGHV14800.pdf

[27] RFHIC. *RRP27311K0-22; 1kW S-band Pulsed Pallet Amplifier*. Datasheet, 2026. [Online] Cited 2026-03-22. Available at: https://rfhic.com/wp-content/uploads/2026/03/RRP27311K0-22_V0.2-1kW-2.7-_-3.1GHz-GaN-Solid-State-Power-Amplifier-SSPA.datasheet-download.pdf

[28] RICHARDS, M. A. *Fundamentals of Radar Signal Processing*. 1st ed. New York: McGraw-Hill, 2005. ISBN: 9780071444743

[29] KHALILPOUR, J., RANJBAR, J., KARAMI, P. A novel algorithm in a linear phased array system for side lobe and grating lobe level reduction with large element spacing. *Analog Integrated Circuits and Signal Processing*, 2020, vol. 104, no. 3, p. 265–275. DOI: 10.1007/s10470-020-01612-1

[30] SKOLNIK, M. I. *Radar Handbook.* 3rd ed. McGraw-Hill, 2008. ISBN: 9780071485470

[31] BALANIS, C. A. *Antenna Theory: Analysis and Design*. 4th ed. John Wiley & Sons, 2016. ISBN-10: 1118642066

[32] ALBERHSEIM, W. J. A closed-form approximation to Robertson's detection characteristics. *Proceedings of the IEEE*, 1981, vol. 69, no. 7, p. 839–839. DOI: 10.1109/PROC.1981.12082

[33] MIT LINCOLN LABORATORY. *Introduction to Radar Systems*. 2020 [Online] Cited 2026-03-22. Available at: https://www.ll.mit.edu/sites/default/files/outreach/doc/2018-07/lecture%203.pdf

[34] PAKFILIZ, A. G. *Self-Protection Jammer Systems*. Artech House, 2024. ISBN-10: 1685690114

[35] LU, X., HUANG, J., WU, Y., et al. Influence of stealth aircraft dynamic RCS peak on radar detection probability. *Chinese Journal of Aeronautics*, 2023, vol. 36, no. 3, p. 137–145. DOI: 10.1016/j.cja.2022.04.009

[36] LU, S., MENG, Z., HUANG, J., et al. Study on quantum radar detection probability based on flying-wing stealth aircraft. *Sensors*, 2022, vol. 22, p. 1–34. DOI: 10.3390/s22165944

[37] ZHANG, B., GAO, Y., WANG, J., et al. Design and analysis of a multispectral compatible stealth metamaterial for enhanced stealth across the laser, infrared, and radar spectral bands. *Optics & Laser Technology*, 2025, vol. 187, p. 1–9. DOI: 10.1016/j.optlastec.2025.112902

About the Author …

Ahmet Güngör PAKFILIZ was born in Turkey. He received his B.S. in Electrical Engineering from Yildiz Technical University in 1991 and his M.Sc. in Electrical and Electronics Engineering from Middle East Technical University in 1997. He achieved his Ph.D. in Electronics Engineering from Ankara University in 2004. His research interests include electronic warfare, radar theory, avionics, and statistical signal processing.